RESEARCH ARTICLE | OCTOBER 03 2024

Drag coefficient of bent-awn plumegrass (*Saccharum contortum*) seeds in wind

Farzad Faraji Dizaji ; Binbin Wang ; Lauren L. Sullivan ; Elizabeth A. Kellogg

Physics of Fluids 36, 101905 (2024)
https://doi.org/10.1063/5.0231717

Physics of Fluids ARTICLE pubs.aip.org/aip/pof

Drag coefficient of bent-awn plumegrass (*Saccharum contortum*) seeds in wind

Cite as: Phys. Fluids **36**, 101905 (2024); doi: 10.1063/5.0231717
Submitted: 1 August 2024 · Accepted: 10 September 2024 ·
Published Online: 3 October 2024

Farzad Faraji Dizaji,[1] Binbin Wang,[1,2,a)] Lauren L. Sullivan,[3,4,5] and Elizabeth A. Kellogg[6,7]

AFFILIATIONS

[1]Department of Civil and Environmental Engineering, University of Missouri, Columbia, Missouri 65211, USA
[2]Missouri Water Center, Columbia, Missouri 65211, USA
[3]Department of Plant Biology, Michigan State University, East Lansing, Michigan 48824, USA
[4]W. K. Kellogg Biological Station, Michigan State University, Hickory Corners, Michigan 49060, USA
[5]Ecology, Evolution and Behavior Program, Michigan State University, East Lansing, Michigan 48824, USA
[6]Donald Danforth Plant Science Center, St. Louis, Missouri 63132, USA
[7]Arnold Arboretum of Harvard University, Boston, Massachusetts 02130, USA

[a)]**Author to whom correspondence should be addressed:** wangbinb@missouri.edu

ABSTRACT

We present a combination of laboratory experiments and computational fluid dynamics (CFD) simulations to understand the wind-induced drag force and drag coefficient for *Saccharum contortum* seeds. Seed drop experiments indicate that the settling fall velocities of hair-equipped seeds are within 1–2 m/s, compared to 2.34 times higher settling fall velocity of the seed without hairs. The experimental data illustrate a power-law relationship between drag coefficient (C_d) and Reynolds number (Re) under the free fall condition: $C_d \sim Re^{-1.1}$. CFD simulations show that both viscous and pressure drag force components are important in contributing to wind drag. The presence of hairs substantially increases pressure drag, and its relative importance depends on hair number and orientation. Seed morphology including hair number and orientation influences the drag coefficient under different flow directions relatively to the seed body. The lower drag coefficient observed with crossflow wind compared to free fall suggests that seeds encounter less air resistance while drifting horizontally in the wind, favoring extended flying time and distance. Based on the varying drag coefficients under different conditions, we propose the incorporation of varying drag coefficients in future wind-driven seed dispersal models.

I. INTRODUCTION

Seed dispersal is a nearly ubiquitous process among plants, which allows for movement between habitats (Damschen *et al.*, 2008; Thompson and Katul, 2008; and Beckman and Sullivan, 2023). While most seeds tend to travel short distances, long-distance-dispersal (LDD) is recognized as a key mechanism for how plants are able to spread over long distances (Clark *et al.*, 1998; Nathan *et al.*, 2002; Fischlin *et al.*, 2007; Soons and Bullock, 2008; and Heydel *et al.*, 2014), which promotes their ability to colonize suitable habitat and adapt as environments continue to change (Corlett and Westcott, 2013; Petersen and Kellogg, 2022).

One common mode of seed dispersal is anemochory or dispersal by wind (Vittoz and Engler, 2007). An essential factor for wind-dispersed seeds to travel long distances is their ability to remain airborne for extended periods. Various flight mechanisms are found for different seed morphologies to facilitate prolonged airborne duration (Seale and Nakayama, 2020). For instance, winged maple seeds and Dipterocarpaceae seeds auto rotate and generate helicopter-like lift as they fall, owing to their optimized shape, size, and angle of attack (aoa) (Fauli *et al.*, 2019; Lentink *et al.*, 2009; Rabault *et al.*, 2019; and Varshney *et al.*, 2012). The lift force is perpendicular to the wind loading, which generates additional drag force in the seed falling direction. In contrast, bristles or hairs may form a parachute-like structure such as the pappus of many Asteraceae diaspores, e.g., dandelion. The pappus reduces the air passing through and sometimes generates a stable separated vortex ring (SVR), which substantially increases the drag force (Cummins *et al.*, 2018; Ledda *et al.*, 2019; and Qiu *et al.*, 2020, 2021, 2022). The impact of seed morphology on the fluid dynamics of flying seeds is profound during wind-driven dispersal.

The unique features of fluid dynamics for flying hair-equipped seeds have been extensively studied for dandelion in recent years with computational fluid dynamics (CFD) tools. The CFD simulations

reproduced the observed SVR in the dandelion wakes and confirmed the enhanced drag in the low Reynolds number regime (Dong *et al.*, 2021). The wake structure of the dandelion seed pappus and the width of the recirculation region in the wake are highly related to the width and density of hairs (Li *et al.*, 2021). A power law was found between drag coefficient (C_D) and Reynolds number (Re) for dandelion seeds: $C_D \sim Re^{-2/3}$ (Sun and Guo, 2023), agreeing with experimental data (Cummins *et al.*, 2018). Furthermore, the shape of SVRs is affected by pappus angle, where a smaller angle can increase the radial pressure gradient toward the central axis of the pappus (Qiu *et al.*, 2022). Flight stability has also been studied using CFD to further understand the role of fine-scale seed morphology (Ledda *et al.*, 2019; Qin *et al.*, 2023). These numerical investigations have been complementary to experimental studies that directly reveal the flow patterns and the flight mechanism (Cummins *et al.*, 2018; Lee *et al.*, 2020) and further expand the available data in the literature.

In contrast, the flight dynamics of grass seeds are not well understood, although many grass seeds are equipped with hairs. Grasses are ubiquitous components of the natural and human-influenced environment, covering as much as 40% of the Earth's land surface (Gibson, 2009). This global distribution reflects their ability to disperse their seeds. While the major domesticated grasses have been selected for their large seeds and high nutritional value, most of the more than 11 000 species of grasses have tiny seeds, which may be subject to dispersal by wind. The seeds are enclosed in papery leaf-like structures or bracts (glumes and lemmas), one of which bears a long tail-like appendage known as an awn; together the seed plus the bracts and awn form the spikelet, which is the dispersal unit. Here, we will use the term "seed" interchangeable with the term "spikelet" as a convenient and easily understood shorthand. The bracts, and in some species the awns, are often decorated with hairs of various lengths, borne in various patterns that are species-specific.

While the hair-covered spikelets of many grasses are reminiscent of the seeds of a dandelion, there are important differences. Notably, the dandelion fruit is radially symmetrical, with the stiff hairs (pappus) interlocking to form a stiff mesh when fully dry. In contrast, the hairs on most grass spikelets are soft and irregularly placed, with variable length and thickness. The spikelet itself is a somewhat irregular shape, often more or less flattened, and the angle of the awn can be highly variable. While hair, awn, and seed morphology are qualitatively described in the literature, it remains unclear what the role is of this fine-scale morphology on the flying dynamics and the impact on the wind-driven dispersal (Petersen and Kellogg, 2022). Considering the grass family's significance as a primary source of human caloric intake (e.g., sugarcane, rice, maize, and wheat) (Kaggwa *et al.*, 2021), its extensive geographic coverage, and the grassland ecosystem's dominance by wind dispersal (Lorts *et al.*, 2008), gaining insights into the wind-driven processes of grassland seed movement is crucial for enhancing our understanding of both ecology and agriculture. Aside from their ecological importance, the irregular shape and complex decoration of grass spikelets makes them interesting in their own right for modeling the fluid dynamics of their dispersal through air. They provide a valuable contrast to better studied shapes and even to the more regularly symmetrical dandelion.

This study will focus on the grassland seeds and investigate the fluid dynamics in free fall and wind dispersal using a bent-awn plumegrass, *Saccharum contortum*. *Saccharum contortum* (also known as *Saccharum brevibarbe* var. *contortum* or *Erianthus contortus*) is a large perennial grass native to the southeastern U.S. (Webster and Shaw, 1995). The plants grow in open sandy habitats and can reach a height of 2.5 m. A striking feature of the spikelet is the dense ring of slender hairs at the base. The hairs are about the same length as the spikelet or slightly shorter. These long dense hairs give the inflorescence of the plant a feathery plume-like appearance, hence the common name plume grass. To characterize the free-falling parameters of *Saccharum contortum* seeds and the flow dynamics in wind-driven dispersal, we carried out a seed drop experiment and a series of CFD simulation of modeled seeds. The objective of the seed drop experiment is to measure the terminal free fall velocity and to examine its relationship with seed mass. The data are also used to determine the drag coefficient as a function of Reynolds number during the free fall condition. The CFD simulation is used to assess the effect of hair morphology, including hair number and orientation on the seed drag at various wind conditions.

II. METHODS

A. Seed drop experiment

The seed drop experiments were conducted to measure the terminal falling velocity of seeds under quiescent conditions using shadow-graphic imaging in the environmental fluid dynamics laboratory at the University of Missouri (Fig. 1). The presented dataset for ten *Saccharum contortum* seeds in this paper is a part of a larger study of 28 different species across the grassland seed tribe. The 10 seeds used in this study were harvested from a *Saccharum contortum* plant that was obtained from Ian Caton at Wood Thrush Natives in Kinsale, VA, a nursery and supplier of native plants. The plant was subsequently grown to flowering in a greenhouse at the Donald Danforth Plant Science Center in St. Louis, MO, under a 14-h day length, with daytime temperatures of 25 °C, nighttime temperatures of 20 °C, and relative humidity ranging from 40% to 90%. The experimental results for *Saccharum contortum* were later used to design CFD simulation. Prior to the drop experiment, the mass of each seed was measured using an ultra micro balance with a precision of 10^{-6} gram. The seeds were not treated or modified during the experiments.

1. Measurement of terminal free fall velocity

Seeds were released from approximately 2 m height using a mailing tube affixed to an enclosed hexagon-shaped glass tank (Fig. 1). This configuration allows an adequate distance for seeds to reach their terminal falling velocity when passing through the field of view (FOV) of the cameras (approximately 20 cm above the tank bottom). Using the terminal velocity of 1.97 m/s as an example (the fastest velocity for seeds with hairs, see Sec. III), a free fall simulation (Wang *et al.*, 2023) suggests that it takes approximately 0.5 s for the seed to reach this velocity, covering a falling distance of approximately 1 m, i.e., 80 cm above the measurement region. For the seed without hairs, the measured velocity is 3.26 m/s. Our simulation suggests that if the terminal velocity is 3.34 m/s, it would take approximately 0.76 s to pass through the imaging location from a 2 m release point at a velocity of 3.26 m/s. Therefore, we estimate a measurement error of about 2% for that seed.

Two LED arrays were placed at the opposite side of the tank for backlighting. Two translucent plates were used to diffuse the light to

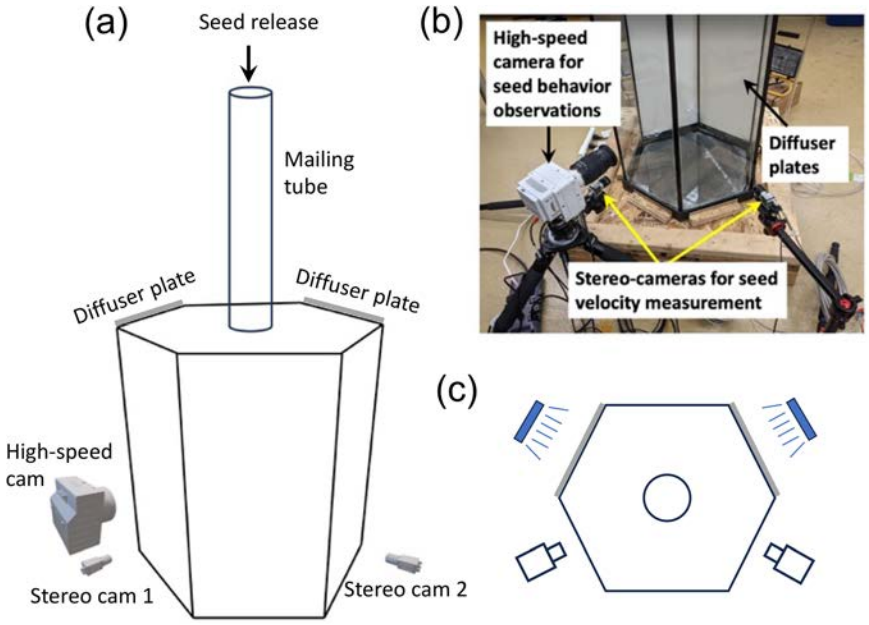

FIG. 1. (a) Sketch of set-up for the seed drop experiment; (b) a photo of the hexagon-shaped glass tank and set-up of the three cameras; and (c) top-view of the experimental set-up.

generate uniform background in the images. The experiment was conducted at a room temperature of approximately 22 °C. The LED lights may have generated some heat, potentially raising the air temperature and altering the humidity in the measurement region. However, temperature and humidity were not monitored. Since the experiment was conducted on the same day, we expect the variation in the effects of temperature and humidity on individual seeds to be minimal. Additionally, ambient noise was minimized to reduce any potential impact on the seed drop experiment.

Two USB 3.0 cameras (Basler acA1300-200um) and a high-speed camera (Vision Research Phantom VEO440L) were placed at two sides of the tank, allowing stereoscopic imaging of the falling seeds. The two USB cameras were synchronized using an external trigger at a sample rate of 50 Hz generated from an Arduino Uno board, where the sample rate varied for each species. The high-speed camera was triggered once the seed was within the FOV at the sample rate of 1100 Hz. The images from two USB cameras were saved directly to the solid-state drive of the operational computer, while the images from the Phantom high-speed camera were initially saved on its 72-GB onboard memory and later transferred to a computer. The cameras were pre-calibrated using a checkerboard before each experiment. Using methodology developed for bubble tracking in the laboratory and in the field, we computed the terminal velocity of seed falling from the three-dimensional coordinates resolved using stereoscopic imaging, averaged from all instantaneous velocities obtained from each pair of consecutive images (Wang and Socolofsky, 2015; Wang *et al.*, 2016, 2020). For each seed, the final terminal velocity value was averaged from five repeated drops. The current study focuses on the terminal velocity of falling seeds, which is used to derive the mean drag coefficient during the terminal falling stage. These average parameters are the focus of the current study because of their importance in seed dispersal models. Variations in instantaneous velocities due to dynamic flow patterns around the seed body will be investigated in future research.

2. Measurement of projected area

To measure the projected area of seeds along the seed falling direction, we set-up the high-speed camera with an upward-facing macro lens, allowing seeds to free fall from approximately 30 cm above the camera [Fig. 2(a)]. A 28-cm long circular-shaped tube was retrofitted to the lens to guide the falling region of the seeds. Similar to the terminal velocity measurement, a downward backlighting set-up was used to perform shadow imaging with a camera frame rate of 1100 Hz [Fig. 2(b)]. The shadow-images were processed using a combined thresholding and edge detection method [Fig. 2(c)] to estimate the projected area (Wang and Socolofsky, 2015). Each seed was dropped five times to obtain an averaged value for the projected area.

B. Seed parameters and modeled seeds

Seed parameters are estimated from the imaging data and later used to generate model for CFD simulations. Figure 3(a) shows a sample image, giving several key parameters: the seed body diameter of 1.36 mm, body length of 8.8 mm, awn length of 15.3 mm, and the longest hair length of 6.5 mm. The sample seed in Fig. 3 has an awn with approximately 100 μm diameter at the tail, increasing in size toward the main body. Within 5.78 mm in length from its tail, the diameter increases from 100 to 190 μm and reaches approximately 330 μm close to the main body. Additionally, scanning electron microscope (SEM, JEOL JSM-6010 LV) images were used to observe the structure and density of the hairs. The SEM images reveal two distinct groups of hairs: short hairs that are closely attached near the base, and long hairs that are more distributed across the body. These long hairs exhibit significant variation in length and angle relative to the seed body. A total of 118 long hairs were counted on the seed shown in Fig. 3(a).

A series of model seeds was generated using the following parameters based on the measured seed dimension from ten seeds: main body length $l_1 = 10.8$ mm and awn length $l_2 = 13.2$, giving the total

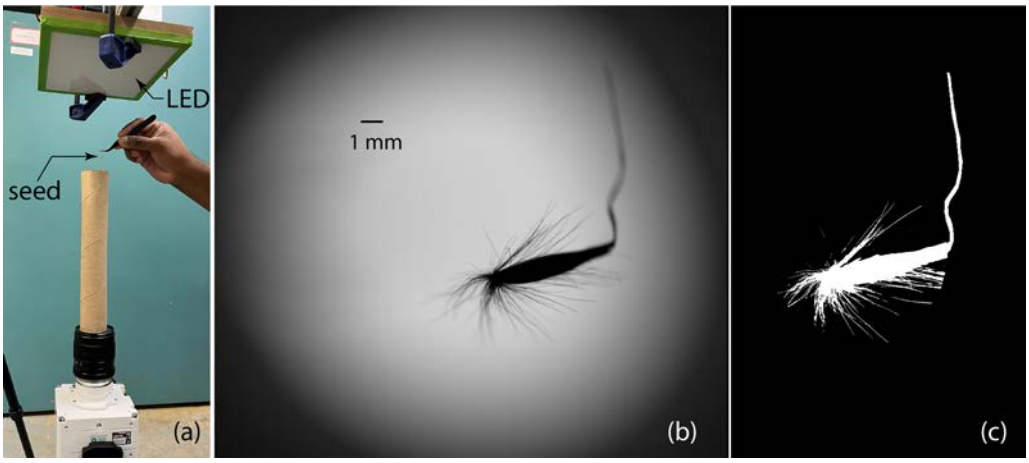

FIG. 2. (a) Set-up of the projected area measurement. (b) An example of imaged seed while falling toward the camera. (c) The processed binary image for estimating the projected area along the falling direction.

length of 24 mm [Fig. 3(b)]. The main body is streamline shaped, with the minimal diameter at the base $d_1 = 0.4$ mm [Fig. 3(c)] and the maximal diameter in the center $d_2 = 1.36$ mm. The awn is slightly curved, shrinking in diameter from the main body to the end, with the center diameter $d_3 = 120$ μm. The hair diameter is $d_0 = 20$ μm, and the diameter of the hair plane is $D = 13.6$ mm when they are perpendicular to the main body ($\theta = 90°$) [Figs. 3(c) and 3(d)].

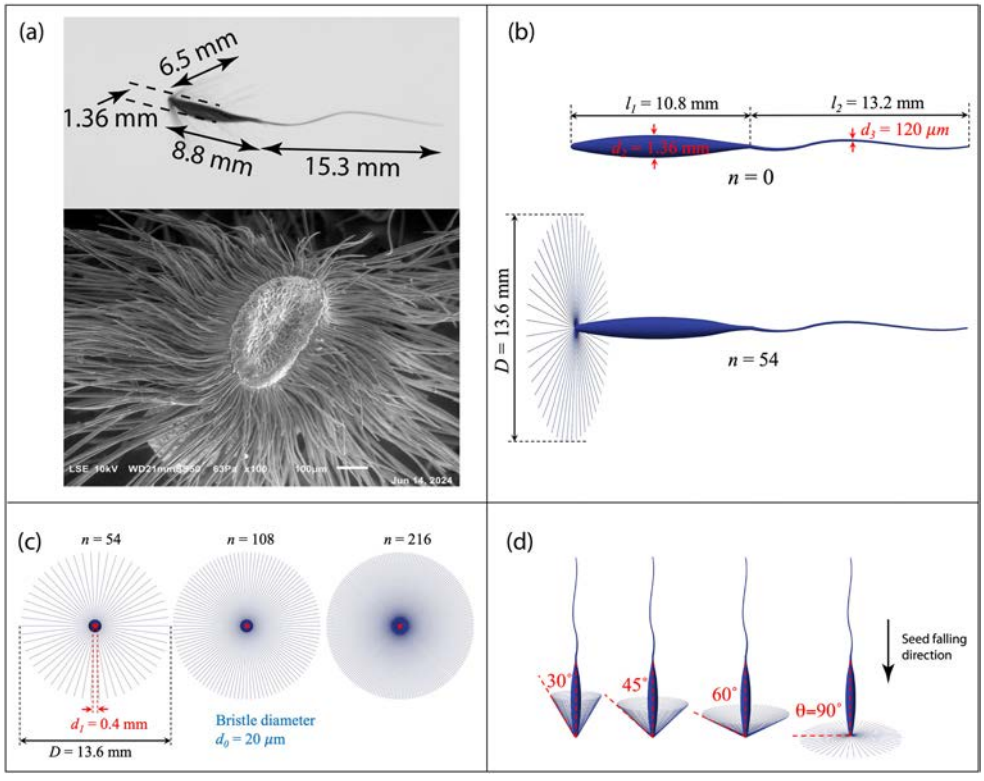

FIG. 3. (a) Photos of a sample *Saccharum contortum* seed and a scanning electron microscope (SEM) image from the base of the seed. The representative key dimensions are measured: length of main body ($l_1 \approx 8.8$ mm), length of awn ($l_2 \approx 15.3$ mm), length of hair ($D/2 \approx 6.5$ mm), diameter of main body ($d_2 \approx 1.36$ mm), and variation in diameter of awn (d_3, ranging from 100 to 330 μm). (b) Two model seeds (one without hairs, one with 54 hairs where the hair plane is perpendicular to the seed body) with dimension shown in the figure. (c) Front view at the seed base with different hair numbers ($n = 54$, 108 and 216). (d) Model seeds with different orientations of the hairs relatively to the seed body. Hair number $n = 128$.

In our simulation, the number of $n = 128$ for the longest hairs is chosen to represent a seed with moderate hair number based on hair counting. The short hairs are not considered in the current study. Additionally, simulations with half and double this number of hairs are conducted for reference [$n = 54$, 128, and 216, Fig. 3(c)]. For the seed of $n = 128$, four different θ values ($\theta = 30°, 45°, 60°$, and 90°) were examined, where θ is the angle between the hair and the seed body [Fig. 3(d)].

C. CFD model

OpenFOAM-6 software package was used to model flow characteristics in steady-state conditions. Steady-state simulation was chosen for this study because it focuses on the wind drag on seeds rather than dynamic flow patterns. Both laminar and turbulent modules were evaluated to determine the drag force and the drag coefficient in various wind conditions because both flow regimes could be present due to the slender body equipped with hairs that occupy a relatively large area. The results indicate that both modules yielded similar results (within 1% difference in drag coefficient). Therefore, all results presented in this paper are the cases of laminar flow simulation.

1. Governing equations

In the laminar module, the continuity equation and the momentum equation (known as governing equations) for steady, incompressible fluid flows are given as follows:

$$\frac{\partial u_i}{\partial x_i} = 0, \tag{1}$$

$$u_j \frac{\partial u_i}{\partial x_j} = -\frac{1}{\rho}\frac{\partial p}{\partial x_j} + \nu \frac{\partial^2 u_i}{\partial x_j \partial x_j}, \tag{2}$$

where u_i and x_i are the velocity and location of the fluid, respectively, with the subscripts $i, j = 1, 2, 3$ representing three directions in the Cartesian coordinate system. p is the pressure, and ρ and ν are the density and the kinematic viscosity of air, respectively.

In the turbulence module, the governing equations are those to determine the mean flow

$$\frac{\partial \overline{u}_i}{\partial x_i} = 0, \tag{3}$$

$$\overline{u}_j \frac{\partial \overline{u}_i}{\partial x_j} = \frac{1}{\rho}\frac{\partial}{\partial x_j}\left(-p\delta_{ij} + 2\mu \overline{S}_{ij} - \rho \overline{u_i' u_j'}\right), \tag{4}$$

where $\overline{u}_i$ is the mean flow velocity in the Cartesian coordinate system, with $\overline{X}$ is the mean of the variable X. $\mu = \rho\nu$ is the dynamic viscosity of air, and $\overline{S}_{ij}$ is the mean strain tensor, defined as $\overline{S}_{ij} = \frac{1}{2}\left(\frac{\partial \overline{u}_i}{\partial x_j} + \frac{\partial \overline{u}_j}{\partial x_i}\right)$.

The k–ω shear stress transport (SST) sub-model was used to close the turbulent fluctuation terms in the equations of motions. The governing equations for turbulence kinetic energy (k) and specific dissipation rate (ω) are given (Menter *et al.*, 2003) as follows:

$$\frac{\partial \rho \overline{u}_i k}{\partial x_i} = P_k - \beta^* \rho \omega k + \frac{\partial}{\partial x_i}\left[(\mu + \sigma_k \mu_t)\frac{\partial k}{\partial x_i}\right] + S_k, \tag{5}$$

$$\frac{\partial \rho \overline{u}_i \omega}{\partial x_i} = \alpha \rho S^2 - \beta \rho \omega^2 + \frac{\partial}{\partial x_i}\left[(\mu + \sigma_\omega \mu_t)\frac{\partial \omega}{\partial x_i}\right] + 2(1 - F_1)\rho \sigma_{\omega 2}\frac{1}{\omega}\frac{\partial k}{\partial x_i}\frac{\partial \omega}{\partial x_i} + S_\omega, \tag{6}$$

where P_k is the production of k due to mean velocity shear, S is the invariant measure of strain rate, and S_k and S_ω are user-defined source terms for k and ω, respectively. Model coefficients including α and β vary using a blending function determined from two sets of coefficients based on the k–ε and k–ω models (e.g., α_1, β_1, α_2, and β_2) (Menter *et al.*, 2003).

In the ω equation, F_1 is the so-called blending function, which is switched in [0,1] depending on the distance to the nearest wall (y) to determine which turbulence model is used. When y is away from the surface, $F_1 = 0$ is used, indicating that the k–ε model is employed. Inside the boundary layer, the k–ω model is used and $F_1 = 1$. All coefficients are determined from the choice of k–ε and k–ω models by the blending function $\alpha = \alpha_1 F_1 + \alpha_2(1 - F_1)$. The default constants are used: $\beta^* = 0.09$, $\alpha_1 = 5/9$, $\beta_1 = 0.075$, $\sigma_{k1} = 0.85$, $\sigma_{\omega 1} = 0.5$, $\alpha_2 = 0.44$, $\beta_2 = 0.0828$, $\sigma_{k2} = 1$, and $\sigma_{\omega 2} = 0.856$ (Menter *et al.*, 2003).

The turbulent viscosity is determined from (Menter *et al.*, 2003)

$$\mu_t = \frac{\rho a_1 k}{\max(a_1 \omega, b_1 F_2 S)}, \tag{7}$$

where $a_1 = 0.31$, $b_1 = 1.0$, and the blending function F_2 is defined as

$$F_2 = \tanh\left[\left(\max\left(\frac{2\sqrt{k}}{\beta^* \omega y}, \frac{500\nu}{y^2 \omega}\right)\right)^2\right]. \tag{8}$$

In the model, the second order Gaussian integration linear method was used for determining gradient and Laplacian operations. Second order Gaussian integration with a linear upwind scheme was used for determining divergence operations.

2. Model domain and boundary condition

The computational domain of $0.05 \times 0.05 \times 0.2$ m^3 ($x \times y \times z$) was used for CFD simulation, where $-z$ is aligned with the seed falling direction (Fig. 4). The domain is approximately 36.7 times the seed body size in the x and y directions, insuring unconstrained boundary. Although the seed hairs span a large area, the flow around them is primarily laminar as a result of small hair diameter. In our simulation conditions, the Reynolds number defined using hair diameter $Re_0 = d_0 U/\nu < 100$, where U is the flow velocity, d_0 is the hair diameter, and ν is the kinematic viscosity of air. The seed was placed at 4 cm from the inlet, allowing adequate distance in both upstream and downstream directions for flow simulation to develop and stabilize. The four sides were set to slip boundary condition. The inlet boundary condition was set at $z = 0$ using constant velocity in the z direction (upward flow). An outlet condition was selected at $z = 0.2$ m for the simulated flow to be fully developed. Five velocity values ($U = 1$, 1.5, 2, 2.5, and 3.26 m/s) were used, based on the seed drop experiment. If the inlet velocity matches the terminal velocity of free fall, it represents the free fall condition. Other velocity values represent the conditions in which air flows in the opposite direction of seed falling. In our

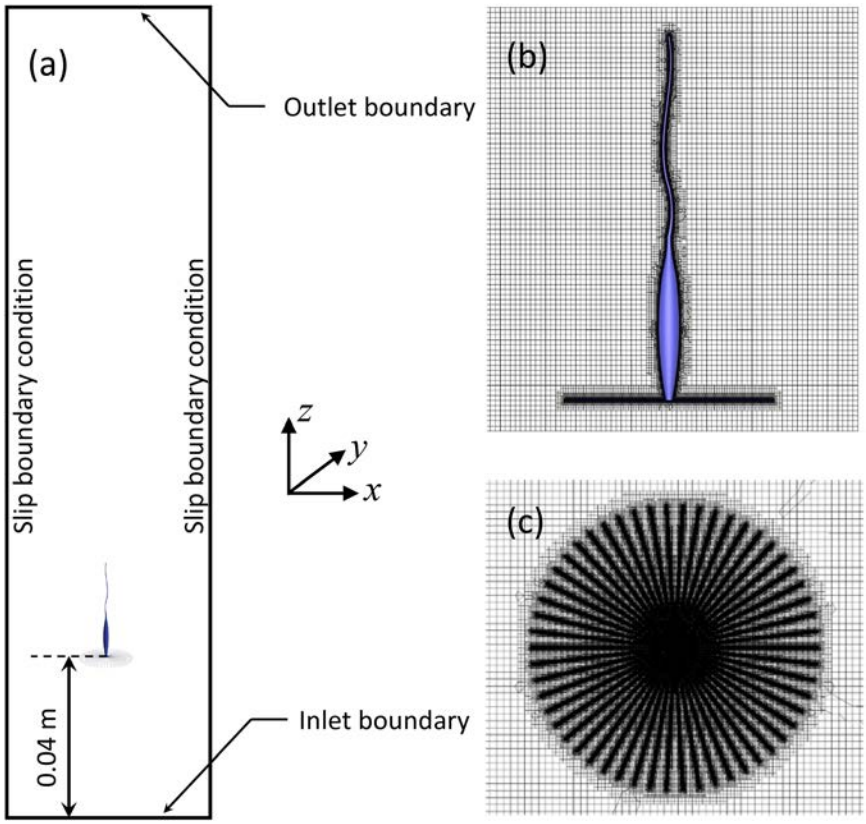

FIG. 4. (a) Sketch of model domain in the $x-z$ plane. (b) Zoom-in view of the mesh around the seed body in the $x-z$ plane. (c) Zoom-in view of the mesh close to the hair in the $x-y$ plane. Shown is the seed with 54 hairs that are perpendicular to the body, i.e., $n = 54$, $\theta = 90^{\circ}$.

modeling, most cases have larger velocities than measured free fall terminal velocities. These cases represent updraft wind in seed dispersal.

In addition, we also simulated the flow conditions where air velocity is in the x (cross flow) and $-z$ directions (downward flow). They represent horizontal and downdraft wind, respectively. The same wind speeds were simulated. Under these conditions, the computational domain and boundary conditions were modified accordingly (by rotating the seed in the domain or moving the seed to the other end of the domain) so that the simulated flow field was not affected by the boundaries. Simulations were conducted on the high performance computing (HPC) environment, Lewis (128 CPUs and 256GB RAM) on the University of Missouri campus.

3. Mesh independence

A mesh independence study was performed prior to simulations. The seed with 54 hairs at $\theta = 90^{\circ}$ was used to assess mesh independence. Four different mesh conditions were assessed: coarse (cell number $= 7.26 \times 10^6$), medium (13.88×10^6), fine (16.63×10^6), and very fine (32.78×10^6). For each mesh condition, we carefully inspected the region around the seed to ensure that all hairs and the mesh around them are rendered correctly. All five velocity conditions were simulated, and total drag force and drag coefficient were calculated for each case. The results indicate that medium, fine, and very fine mesh yielded similar output, while coarse mesh yielded smaller drag force, hence smaller drag coefficient (Fig. 5). With very fine mesh as the reference, the relative error for coarse, medium, and fine mesh was 6%, 0.2%, and 0.6%, respectively. Therefore, we chose medium mesh as our final model mesh. With this mesh condition, the minimal and maximal cell volume are 1.18×10^{-18} and 3.72×10^{-11} m^3,

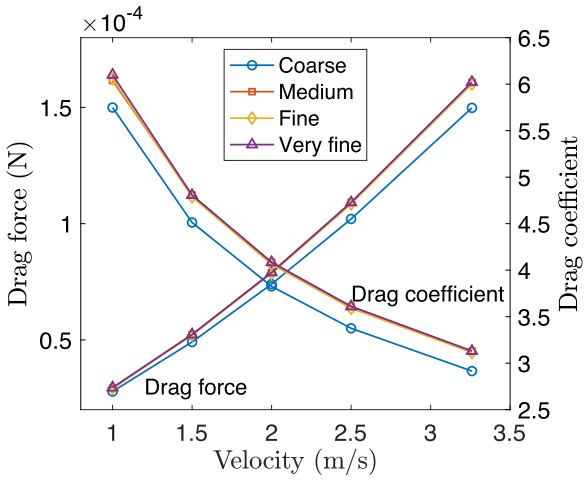

FIG. 5. Mesh independence study for the seed ($n = 54$, $\theta = 90^{\circ}$). The relative errors in the drag force and drag coefficient for coarse, medium, and fine mesh compared to the very fine mesh are 6%, 0.2%, and 0.5%, respectively.

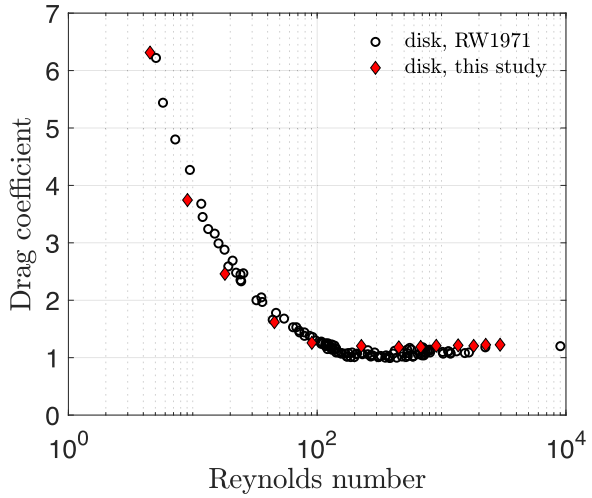

FIG. 6. Comparison between modeled results and experimental data for the drag coefficient of disk as a function of Reynolds number. The experimental data are from Roos and Willmarth (1971). RMSE in drag coefficient between the experiment and model is 0.068.

respectively. The maximal skewness and aspect ratio are 2.9 and 21.57, respectively.

4. Model evaluation

The CFD model was evaluated using flow around a disk for various flow conditions with Reynolds numbers ranging from 4.5 to 2956. We calculated drag coefficient for each case and compared results with experimental data reported in Roos and Willmarth (1971) (Fig. 6). The comparison demonstrates good agreements with a root mean square-error (RMSE) of 0.068 between model and experiment for the tested drag coefficient range of 1.2–6.3.

III. RESULTS

A. Seed drop experiment

The seed drop measurements show the terminal settling velocities for most *Saccharum contortum* seeds are in the range of $1-2$ m/s (Fig. 7). The measured data indicate strong effect of hairs on the terminal velocity, evidenced by the seed #7, which has no hairs on the seed body and exhibits a substantially higher velocity (3.26 m/s).

A positive correlation was found between the mass of seeds (M) and their terminal velocities (V_T), excluding the no-hair seed #7 [Fig. 8(a)]. A best linear function $V_T = 0.59M - 0.41$ can be used to

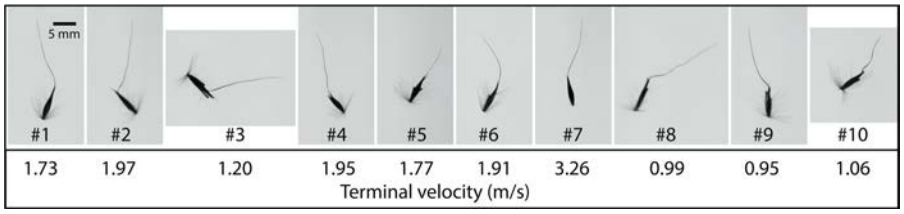

FIG. 7. Image of 10 free-falling *Saccharum contortum* seeds. All seeds are displayed on the same scale. The measured terminal settling velocity is indicated for each seed.

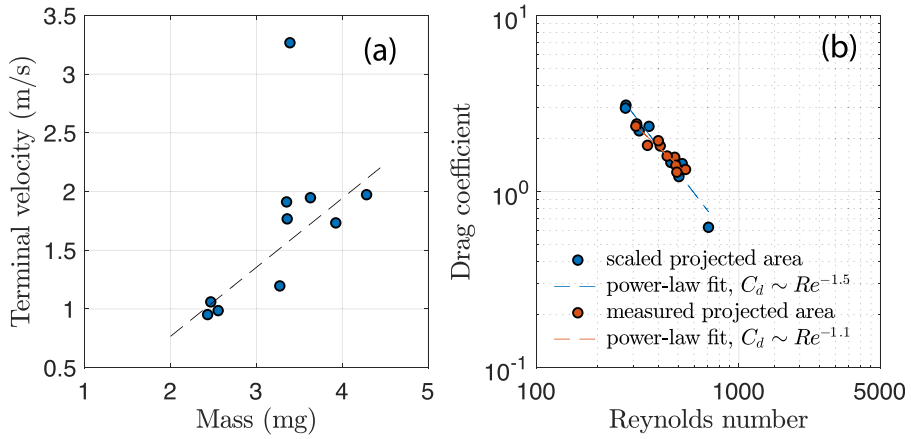

FIG. 8. (a) Measured seed terminal settling velocity as a function of mass. The black dashed line is the best-fit for all seeds but the one without the hairs. The best-fit equation is $V_T = 0.59M - 0.41$, where the units are m/s and mg for terminal velocity (V_T) and mass (M), respectively. (b) Estimated drag coefficient as a function of Reynolds number, defined as $Re = V_T(A_p\pi/4)^{0.5}/\nu$, where A_p is the projected area in the free fall direction. Here, the data of C_d and Re are reported using two different estimates of A_p: the directly measured values (red circles) and the scaled values using the projected area of seeds on the imaging direction ($A_{p,\text{img}}$), i.e., $A_p = f_A A_{p,\text{img}}$ (blue circles), where $f_A = 0.36$ is the scaling factor, i.e., mean ratio of measured $A_p/A_{p,\text{img}}$. The power-law fit shows $C_d \sim Re^{-1.1}$ using the measured A_p and $C_d \sim Re^{-1.5}$ using the scaled A_p.

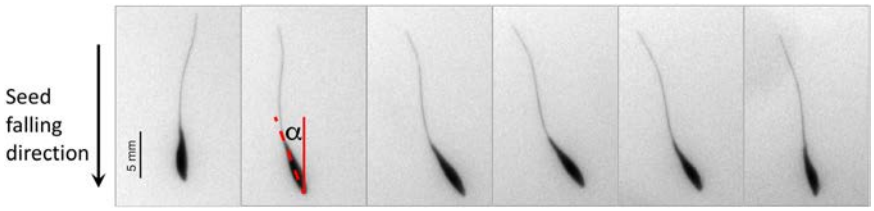

FIG. 9. A sequence of images of seed #7 under free fall condition. The time interval between consecutive images is 0.02 s. The values of α in the images are 0°, 5°, 22°, 33°, 36°, 30°, and 14°.

describe their relationship with V_T in m/s and M in mg. The measured velocities allow us to evaluate the drag coefficient of free-falling seeds. Under the terminal falling stage, the drag force should be balanced by the gravitational force, giving $F_D = Mg$, where g is the gravitational acceleration and F_D is the drag force. Drag force is defined by $F_D = C_d \rho V_T^2 A_P/2$, where C_d is the drag coefficient and A_p is the projected area of seed along the free fall direction (i.e., x–y plane). In our experiment, we can also use a scaling factor to relate A_p with the projected area in the imaging plane, $A_{p,\mathrm{img}}$ (i.e., x–z or y–z plane): $A_p = f_s A_{p,\mathrm{img}}$. With this assumption, we computed Reynolds number $Re = V_T (A_p \pi/4)^{0.5}/\nu$, and the drag coefficient as a function of Re is shown in Fig. 8(b). The data indicate a near power-law relationship, and the best-fit shows $C_d \sim Re^{-1.1}$ using the directly measured A_p and $C_d \sim Re^{-1.5}$ using the scaled A_p.

B. Modeling of seed without hairs

The experimental data of free-falling seed #7 provide us the baseline reference in the simulation of a seed without hairs (Fig. 9). The experimental data indicate that the seed changed its orientation in falling, yielding various angles in the two-dimensional images. The available images indicate that the aoa for seed #7 is approximately 36°. Various seeds may experience various angles of attack during free fall.

To examine the effect of aoa on seed falling dynamics, we simulated the flow around a non-hair seed with seven different aoa (0°–36°) and determined both viscous- and pressure-force components of the drag force (Fig. 10). The simulation results indicate that streamlines were curved due to flow direction changes around the seed body. A wake field formed downstream of the seed body, giving a lower velocity in the wake than the free-stream velocity. A pressure difference occurred near the seed body between the upstream and downstream regions [Figs. 10(a)–10(c)].

The simulation results indicate that the viscous force is dominant for all tested cases for non-hair seeds [Fig. 10(d)]. Both viscous and pressure forces increase with increasing aoa. The pressure force demonstrates a more pronounced response to changes in the aoa compared to the viscous force. With increasing aoa, the pressure force increases by 33 times, while the viscous force increases by 2 times. At aoa = 0°, the pressure force is 4.9% of the viscous force, while it is 81.3% of the viscous force at aoa = 36°.

C. Seed falling and upward wind

The simulation results indicate that the hair numbers significantly affect the flow pattern around the seed body (Fig. 11). With $n = 54$ [Fig. 11(a)], the velocity distribution is near axial symmetric, indicating that the effect of hairs on the flow pattern is small. The boundary layer is mainly developed around the main stem of the seed body. With increasing n, the flow pattern becomes irregularly shaped, depicting the strong impact of hairs on the downstream flow pattern. The size of the low velocity zone increases substantially in the downstream with increasing n value.

The contribution of viscous- and pressure-force components on the drag was examined for the seeds with various hair numbers under different wind speeds (Fig. 12). The results demonstrate that the seeds with hairs have similar viscous and pressure drag at all wind speeds, with the mean pressure to viscous drag ratio to be 1.01 for all three n values (54, 108, and 216). The referencing non-hair seed has the pressure to viscous drag ratio of 0.044.

The relationship between drag coefficient and Reynolds number is given in Fig. 13. Here, two different definitions of Re are used. In

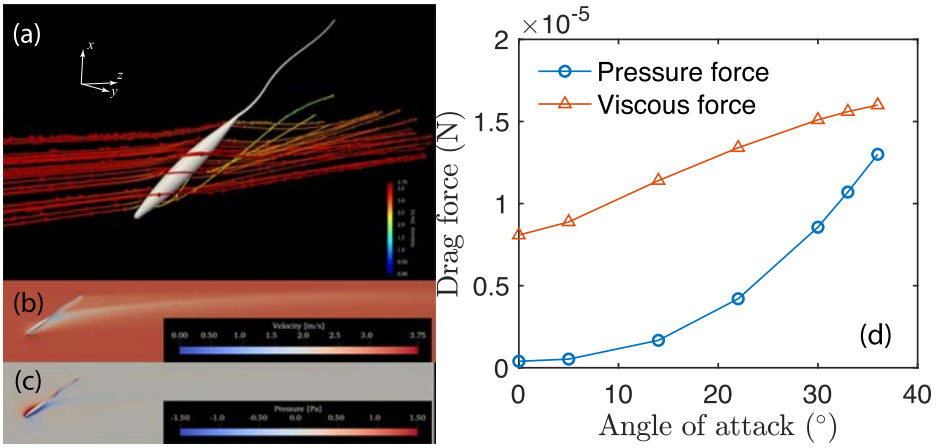

FIG. 10. (a) Streamlines of the flow around the seed body at the angle of attack (aoa) of 36°. Note that the coordinate system is rotated in the plot; (b) velocity field; (c) pressure field; and (d) comparison between the pressure force and the viscous force on the seed without hairs and under different aoa at a wind speed of 3.26 m/s.

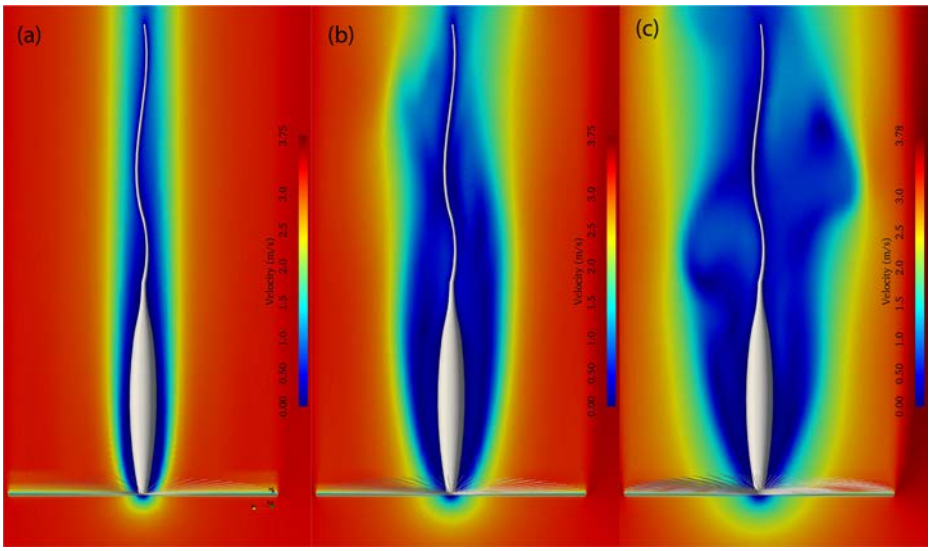

FIG. 11. Velocity field around seed body for three different hair numbers: (a) $n = 54$; (b) $n = 128$; and (c) $n = 216$; the upward wind speed is 3.26 m/s.

Fig. 13(a), Reynolds number is defined based on the diameter of the hair-occupied area (similar to pappus of dandelions) [D, see Fig. 3(a)]. This definition has been used in the literature (Cummins *et al.*, 2018); however, it is higher than the true projected area as defined in drag force due to the porosity of the pappus. For instance, Cummins *et al.* (2018) show that the area of a disk is about 5–7 times of the area of dandelion pappus with the same diameter. With this *Re*, all hair seeds have the same *Re*, showing a much higher drag coefficient with the same *Re* for the disks [Fig. 13(a)].

The second *Re* is defined based on the true projected area along the flow direction, giving $Re = U(4A_p/\pi)^{0.5}/\nu$. With this definition, the drag coefficient for the non-hair seeds falls much closer to the curve of disks than these seeds with hairs (Fig. 13). With increasing hair number, *Re* slightly increases under the wind speed. In general, the hair seeds have much higher drag coefficients than the solid body

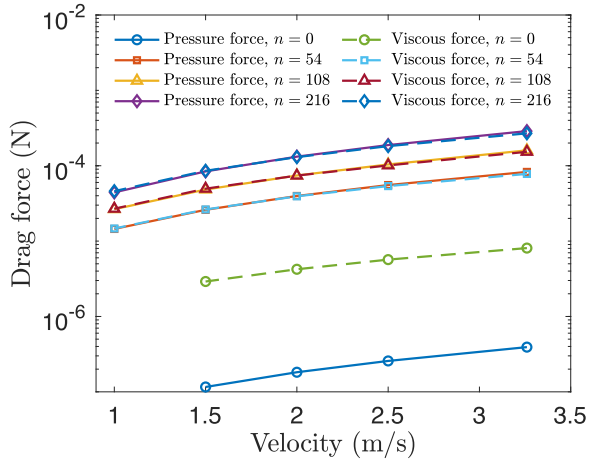

FIG. 12. Comparison between pressure drag and viscous drag on the seeds under different wind speeds and numbers of hairs.

such as disks. The modeled drag coefficients are in the approximate range of 3–6.

We further examined the effect of hair orientation on the drag coefficient as a function of Reynolds number (Fig. 14). The simulation results indicate that decreasing θ leads to decrease in drag coefficient as a function of Reynolds number with the same hair number. The decreasing drag coefficient with decreasing θ is more profound for more hairs. For instance, the drag coefficient becomes almost constant (≈ 1.8) for the seeds at θ in the range of 30°–90° with 216 hairs. For $n = 54$, drag coefficients are in the range of 2.44–4.38 in the same θ range.

D. Crossflow wind

When the wind speed is a crossflow that is perpendicular to the seed falling direction, the drag forces on the seeds in the horizontal direction were determined. Figure 15 displays the drag coefficient for crossflow wind at the same wind speed as that in upward wind. Compared with upward winds, the crossflow winds resulted in much smaller drag coefficients. Drag coefficient still exhibited a decreasing trend with increasing Reynolds number; however, the values of drag coefficients were primarily within the range of 1–2, regardless of the hair orientations, i.e., different θ values.

E. Downward wind

The drag coefficient-Reynolds number relationship is also investigated for downward wind conditions and compared with those observed in upward wind conditions (Fig. 16). At $\theta = 90°$, the drag coefficient in upward wind is slightly higher than that in downward wind. However, for angles between $\theta = 30°$ and $\theta = 60°$, the drag coefficient in upward wind is lower than that in downward wind. At $\theta = 60°$ and $\theta = 90°$, the difference in drag coefficient between upward and downward wind is relatively small. Nonetheless, this difference increases for smaller θ, resulting in a mean drag coefficient ratio of 1.24 between upward and downward winds.

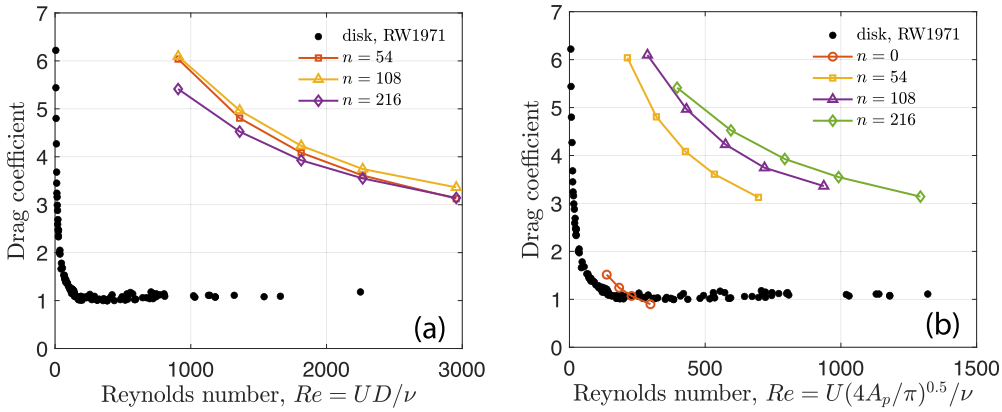

FIG. 13. Drag coefficient as a function of Reynolds number defined using different seed length scales: (a) based on diameter of the spread of the hairs and (b) based on effective diameter determined from projected area. Drag coefficients for disks are plotted for reference (Roos and Willmarth, 1971).

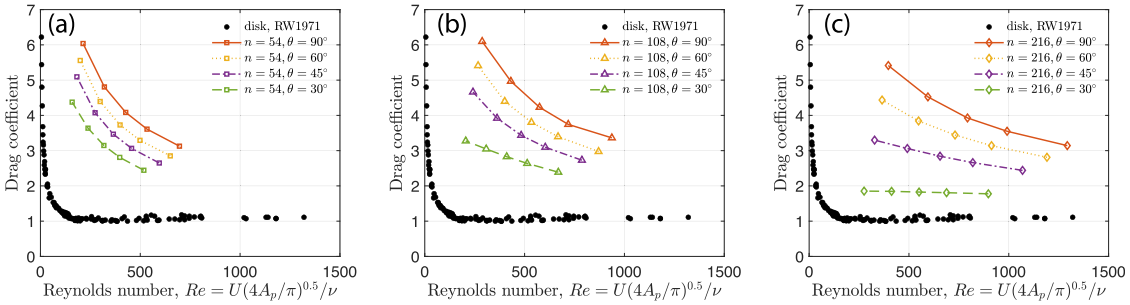

FIG. 14. Drag coefficient as a function of Reynolds number for different hair numbers and different hair orientations relatively to the seed body [i.e., different θ values, see Fig. 3(d) for the definition of θ]: (a) $n = 54$; (b) $n = 108$; and (c) $n = 216$.

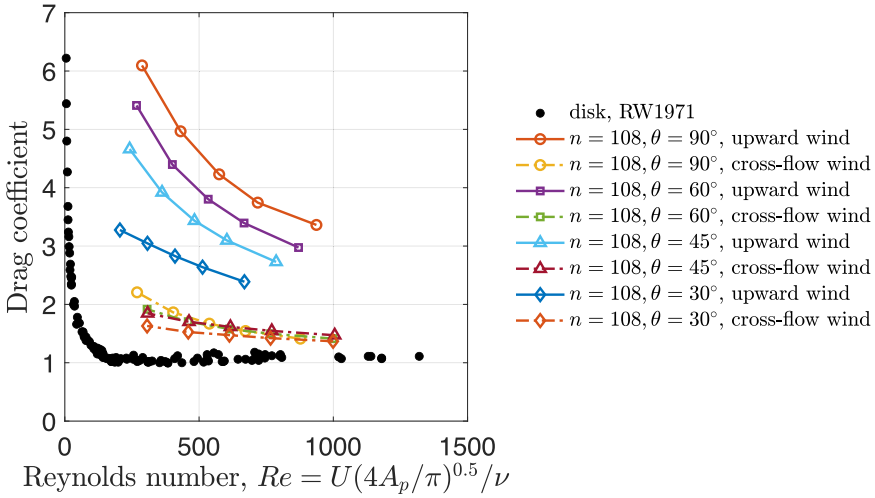

FIG. 15. Drag coefficient as a function of Reynolds number for different θ values in crossflow wind, compared with upward wind.

IV. DISCUSSION

The simulations demonstrate that both viscous- and pressure-force components are important contributors to the total drag on the *Saccharum contortum* seeds. For the seed without hairs, the viscous force component dominates the drag (Fig. 10) at aoa of 0°, indicating that the seed is a streamlined body with negligible wake behind the body, where the drag is primarily caused by the friction inside the boundary layer developed around the seed body. For the seeds with

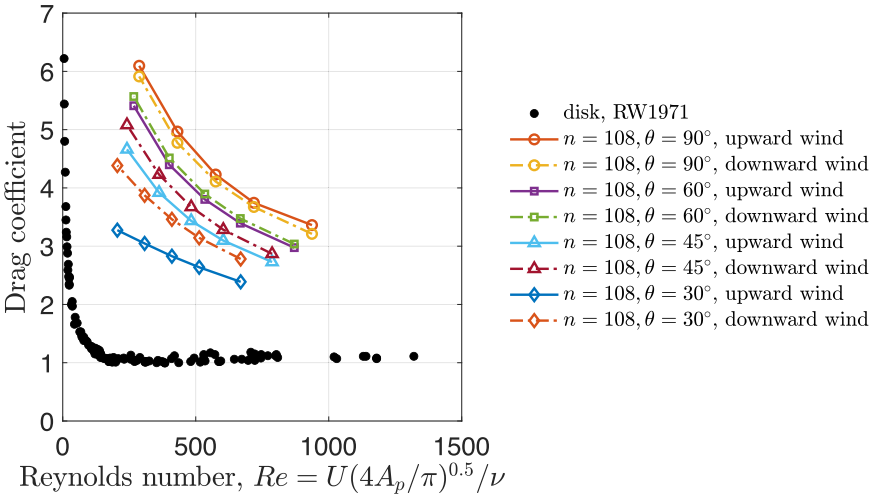

FIG. 16. Drag coefficient as a function of Reynolds number for different θ values in downward wind, compared with upward wind.

hairs, the simulation results depict that both viscous and pressure drags are important (Fig. 12), indicating that both the boundary layer developed around the seed body and the hairs (viscous force contributor) and the eddy motions developed in the wake (pressure force contributor) play similar roles in the drag force. The importance of the viscous force component is also evidenced by the observed strong relationship between drag coefficient with Reynolds number (Fig. 13) because the development of the boundary layer typically scales well with Reynolds number.

For the flows with significant wake and pressure drag, the dependence of the drag coefficient on Reynolds number is less sensitive. In our simulations, we observed that the dependence of the drag coefficient on Reynolds number weakens with decreasing θ value (Fig. 14). The weakening is more obvious in the cases of high hair numbers. For instance, the drag coefficient is almost independent of Reynolds number for the case of $n = 216$ and $\theta = 30°$. We suspect that this is due to the substantial decrease in hair–hair distance with decreasing θ, which may trigger the strong effect of dense hairs on the flow patterns, leading to the substantial reduction of air flow through the void among hairs. The abrupt change in flow pattern and the corresponding effect on drag due to small, densely packed voids were observed in creeping flows around dense slender bodies (Barta and Weihs, 2006) and were believed to play a significant role in helping dandelion to remain aloft (Cummins *et al.*, 2018).

The comparison of simulation results in upward and crossflow winds indicates greater drag experienced by seeds in the vertical direction (including free fall) compared to horizontal wind (Fig. 15). Although this result is intuitive, no data are available in the literature to demonstrate the difference in drag coefficient under the same Reynolds number. Consequently, using a free fall drag coefficient to predict wind-borne seed movement in the horizontal direction inherently introduces error due to the use of an inappropriate value of drag coefficient.

Furthermore, seed drag varies under upward and downward wind conditions. This variation is particularly pronounced when the hairs reorient toward the seed body, resulting in a decrease in the angle θ (Fig. 16). Because wind is highly turbulent, characterized by abrupt and substantial changes in magnitude and direction, seed drag exhibits significant variation as a function of both wind parameters and seed morphology. This variability can introduce substantial uncertainties into seed dispersal models that rely on a constant drag coefficient or other equivalent parameters (e.g., terminal velocity) (Soons *et al.*, 2004; Wang *et al.*, 2023). To improve model accuracy in predicting seed dispersal by wind, we recommend incorporating drag coefficient values that vary based on both wind parameters and seed morphology.

The varying drag coefficients of a seed at different angles relative to the direction of free fall and wind impact dispersal distances. The lower drag coefficient aligned with the wind compared to free fall indicates that seeds encounter less air resistance while drifting horizontally in the wind than when falling vertically. Hence, the fluid dynamics influenced by seed morphology in various flow directions favor longer-distance dispersal of *Saccharum contortum* by wind.

Changes in the orientation of the hairs relative to the body of the seed may greatly influence dispersal distances by wind. For example, for dandelions in humid environments conducive to seed germination, the hairs tend to draw closer to the seed body (i.e., smaller θ) (Seale *et al.*, 2022). It is plausible to assume that the same phenomenon occurs in *Saccharum contortum*, although we have no data to be certain. Our model results indicate that this morphology reduces the drag coefficient during free fall, thus accelerating descent. As a result, seeds can reach the ground more rapidly for germination.

The influence of different drag coefficients in upward and downward wind directions on dispersal distance is nuanced, especially considering the role of hair orientation. Seed dispersal modeling has shown that updraft winds notably contribute to LDD (Nathan *et al.*, 2002). For a seed with a smaller drag coefficient in upward wind compared to downward wind, it could experience less resistance to the force caused by wind load, allowing the seed to be carried upward more efficiently. This flow dynamics feature could lead to increased dispersal heights or distances, depending on other factors such as seed weight and wind strength.

We acknowledge several limitations in our experimental and simulation study that can be addressed in future research. First, increasing the sample size of *Saccharum contortum* in the seed drop experiment would allow for a broader range of variability across individual seeds and lead to better convergence in developing the relationship between

drag coefficient and Reynolds number. Second, temperature and humidity can influence air density and potentially affect seed morphology, which, in turn, could impact terminal velocity and drag coefficient. This effect was not investigated and will be explored in future studies. Additionally, variations in instantaneous velocity are related to the flow pattern and instability around the seed body, which could contribute to wind drag. Understanding how flow instability is related to the fine-scale morphology of seeds is of great interest to the fluid dynamics community.

Additionally, more precise quantitative measurements of seed hairs (e.g., number, length, angle, and their variations) are needed in future studies to create more realistic seed models for numerical simulations. In the current simulations, laminar flow was assumed for all cases, and the wind speed at which the flow may transition to turbulence remains unclear. In natural environments, airflow is typically turbulent and can change direction rapidly. While this study focuses only on vertical and horizontal flow directions, how seeds interact with turbulent wind and how this affects the drag coefficient are important topics for future investigation.

V. CONCLUSIONS

This study investigates seed drag in relation to wind conditions and seed morphology using a combined approach. A laboratory experiment examined the free fall of bent-awn plumegrass (*Saccharum contortum*) seeds. These data informed a computational fluid dynamics (CFD) model simulating idealized wind conditions around the seeds.

The seed drop experiment indicates that the *Saccharum contortum* seeds have a terminal free fall velocity primarily in the range of 1–2 m/s. Among the 10 dropped seeds, the seed lacking hairs exhibited a significantly higher terminal velocity, reaching 2.34 times the average velocity observed in other nine seeds with hairs. For seeds with hairs, terminal velocity exhibited a linear relationship with seed mass, while the drag coefficient displayed a power-law dependence on the Reynolds number.

The CFD simulation demonstrates that the body of *Saccharum contortum* seeds possesses a streamlined shape, with frictional forces within the boundary layer dominating drag during free fall and upward wind conditions. The presence of hairs leads to an increase in pressure drag, suggesting the formation and influence of eddy motions in the wake of seeds. The observed dependence of the drag coefficient on Reynolds number, along with the comparable magnitudes of viscous and pressure forces, highlights the significance of both frictional and pressure variations in the flow field. Seed morphology can significantly impact the relationship between drag coefficient and Reynolds number. Seeds with dense hairs that reorient toward the body exhibit a weaker dependence, potentially due to a stronger wake caused by reduced flow through the hair gaps.

Our simulations reveal a distinct relationship between drag coefficient and Reynolds number depending on wind direction. Seeds experience lower drag in horizontal winds compared to vertical ones, with similar variations observed between upward and downward winds. Seed morphology, particularly hair number and orientation, significantly impacts this drag-Reynolds number relationship across different wind directions. In conclusion, this study quantified the interplay between wind magnitude, direction, and seed morphology (including hair number and orientation) in affecting drag coefficient. To enhance the accuracy of seed dispersal models in wind environments, we advocate for incorporating drag coefficients that dynamically respond to both wind parameters and seed morphology.

ACKNOWLEDGMENTS

We thank the postdocs, graduate, and undergraduate students, including Huijie Wu, Britton Stamps, Dante Nguyen, and Kurt Petersen, for their assistance with the seed drop experiment and creating seed models. This is Kellogg Biological Station Contribution no. 2392.

AUTHOR DECLARATIONS

Conflict of Interest

The authors have no conflicts to disclose.

Author Contributions

Farzad Faraji Dizaji: Data curation (equal); Formal analysis (equal); Investigation (equal); Methodology (equal); Validation (equal); Visualization (equal); Writing – original draft (equal). **Binbin Wang:** Conceptualization (equal); Investigation (equal); Methodology (equal); Resources (equal); Supervision (equal); Writing – original draft (equal); Writing – review & editing (equal). **Lauren L. Sullivan:** Conceptualization (equal); Investigation (equal); Writing – review & editing (equal). **Elizabeth A. Kellogg:** Conceptualization (equal); Writing – review & editing (equal).

DATA AVAILABILITY

The data that support the findings of this study are available from the corresponding author upon reasonable request.

REFERENCES

Barta, E. and Weihs, D., "Creeping flow around a finite row of slender bodies in close proximity," J. Fluid Mech. **551**, 1–17 (2006).
Beckman, N. G. and Sullivan, L. L., "The causes and consequences of seed dispersal," Annu. Rev. Ecol., Evol. Syst. **54**, 403–427 (2023).
Clark, J. S., Fastie, C., Hurtt, G., Jackson, S. T., Johnson, C., King, G. A., Lewis, M., Lynch, J., Pacala, S., Prentice, C., Schupp, E. W., Webb III, T., and Wyckoff, P., "Reid's paradox of rapid: Dispersal theory and interpretation of paleoecological records," BioScience **48**, 13–24 (1998).
Corlett, R. T. and Westcott, D. A., "Will plant movements keep up with climate change?," Trends Ecol. Evol. **28**, 482–488 (2013).
Cummins, C., Seale, M., Macente, A., Certini, D., Mastropaolo, E., Viola, I. M., and Nakayama, N., "A separated vortex ring underlies the flight of the dandelion," Nature **562**, 414–418 (2018).
Damschen, E. I., Brudvig, L. A., Haddad, N. M., Levey, D. J., Orrock, J. L., and Tewksbury, J. J., "The movement ecology and dynamics of plant communities in fragmented landscapes," Proc. Natl. Acad. Sci. U. S. A. **105**, 19078–19083 (2008).
Dong, Y. Y., Hu, K. X., Wang, Y. B., and Zhang, Z. J., "The steady vortex and enhanced drag effects of dandelion seeds immersed in low-Reynolds-number flow," AIP Adv. **11**(8), 085320 (2021).
Fauli, R. A., Rabault, J., and Carlson, A., "Effect of wing fold angles on the terminal descent velocity of double-winged autorotating seeds, fruits, and other diaspores," Phys. Rev. E **100**(1), 013108 (2019).
Fischlin, A., Midgley, G. F., Price, J. T., Leemans, R., Gopal, B., Turley, C., Rounsevell, M. D. A., Dube, O. P., Tarazona, J., and Velichko, A. A., "Ecosystems, their properties, goods, and services," in *Climate Change 2007: Impacts, Adaptation and Vulnerability* (Cambridge University Press, 2007).
Gibson, D. J., *Grasses and Grassland Ecology* (Oxford University Press, 2009).

Heydel, F., Cunze, S., Bernhardt-Römermann, M., and Tackenberg, O., "Long-distance seed dispersal by wind: Disentangling the effects of species traits, vegetation types, vertical turbulence and wind speed," Ecol. Res. **29**, 641–651 (2014).
Kaggwa, R. J., Jiang, H., Ryan, R. A., Zahller, J. P., Kellogg, E. A., Woodford-Thomas, T., and Callis-Duehl, K., "Exploring grass morphology & mutant phenotypes using *Setaria viridis*," Am. Biol. Teach. **83**, 311–319 (2021).
Ledda, P. G., Siconolfi, L., Viola, F., Camarri, S., and Gallaire, F., "Flow dynamics of a dandelion pappus: A linear stability approach," Phys. Rev. Fluids **4**(7), 071901(R) (2019).
Lee, M., Lee, S. H., and Kim, D., "Stabilized motion of a freely falling bristled disk," Phys. Fluids **32**, 113604 (2020).
Lentink, D., Dickson, W. B., van Leeuwen, J. L., and Dickinson, M. H., "Leading-edge vortices elevate lift of autorotating plant seeds," Science **324**, 1438–1440 (2009).
Li, S. Q., Pan, D. Y., Li, J., and Shao, X. M., "Drag and wake structure of a quasi-dandelion pappus model at low and moderate Reynolds numbers: The effects of filament width," Phys. Fluids **33**(12), 121904 (2021).
Lorts, C. M., Briggeman, T., and Sang, T., "Evolution of fruit types and seed dispersal: A phylogenetic and ecological snapshot," J. Syst. Evol. **46**(3), 396–404 (2008).
Menter, F. R., Kuntz, M., and Langtry, R., "Ten years of industrial experience with the SST turbulence model," in *Turbulence, Heat and Mass Transfer* (TIB, 2003), pp. 625–632.
Nathan, R., Katul, G. G., Horn, H. S., Thomas, S. M., Oren, R., Avissar, R., Pacala, S. W., and Levin, S. A., "Mechanisms of long-distance dispersal of seeds by wind," Nature **418**, 409–413 (2002).
Petersen, K. B. and Kellogg, E. A., "Diverse ecological functions and the convergent evolution of grass awns," Am. J. Botany **109**, 1331–1345 (2022).
Qin, L., Jian, Z., Xu, Y. Y., and Ma, L. F., "On the attitude stability of flying dandelion seeds," Phys. Fluids **35**(8), 081904 (2023).
Qiu, F. S., He, T. B., and Bao, W. Y., "Effect of porosity on separated vortex rings of dandelion seeds," Phys. Fluids **32**(11), 113104 (2020).
Qiu, F. S., Qian, H. Y., Du, Y. M., and Li, C. J., "The pappus angle as a key factor in the entire separation of a vortex ring from a dandelion seed's pappus," Phys. Fluids **34**(8), 083101 (2022).
Qiu, F. S., Wang, B. W., Du, Y. M., and Qian, H. Y., "Numerical investigation on the flow characteristics of model dandelion seeds with angles of attitude," Phys. Fluids **33**(11), 113107 (2021).
Rabault, J., Fauli, R. A., and Carlson, A., "Curving to fly: Synthetic adaptation unveils optimal flight performance of whirling fruits," Phys. Rev. Lett. **122**(2), 024501 (2019).
Roos, F. W. and Willmarth, W. W., "Some experimental results on sphere and disk drag," AIAA J. **9**(2), 285–291 (1971).
Seale, M. and Nakayama, N., "From passive to informed: Mechanical mechanisms of seed dispersal," New Phytol. **225**(2), 653–658 (2020).
Seale, M., Zhdanov, O., Soons, M. B., Cummins, C., Kroll, E., Blatt, M. R., Zare-Behtash, H., Busse, A., Mastropaolo, E., Bullock, J. M., Viola, I. M., and Nakayama, N., "Environmental morphing enables informed dispersal of the dandelion diaspore," eLife **11**, e81962 (2022).
Soons, M. B. and Bullock, J. M., "Non-random seed abscission, long-distance wind dispersal and plant migration rates," J. Ecol. **96**, 581–590 (2008).
Soons, M. B., Heil, G. W., Nathan, R., and Katul, G. G., "Determinants of long-distance seed dispersal by wind in grasslands," Ecology **85**, 3056–3068 (2004).
Sun, B. H. and Guo, X. L., "Drag scaling law and parachute terminal velocity of the dandelion," AIP Adv. **13**(8), 085305 (2023).
Thompson, S. and Katul, G., "Plant propagation fronts and wind dispersal: An analytical model to upscale from seconds to decades using superstatistics," Am. Nat. **171**, 468–479 (2008).
Varshney, K., Chang, S., and Wang, Z. J., "The kinematics of falling maple seeds and the initial transition to a helical motion," Nonlinearity **25**, C1 (2012).
Vittoz, P. and Engler, R., "Seed dispersal distances: A typology based on dispersal modes and plant traits," Bot. Helv. **117**, 109–124 (2007).
Wang, B., Jun, I., Socolofsky, S. A., DiMarco, S. F., and Kessler, J. D., "Dynamics of gas bubbles from a submarine hydrocarbon seep within the hydrate stability zone," Geophys. Res. Lett. **47**(18), e2020GL089256, https://doi.org/10.1029/2020GL089256 (2020).
Wang, B. and Socolofsky, S. A., "A deep-sea, high-speed, stereoscopic imaging system for in situ measurement of natural seep bubble and droplet characteristics," Deep Sea Res., Part I **104**, 134–148 (2015).
Wang, B., Socolofsky, S. A., Breier, J. A., and Seewald, J. S., "Observation of bubbles in natural seep flares at MC 118 and GC 600 using in situ quantitative imaging," J. Geophys. Res. **121**, 2203–2230, https://doi.org/10.1002/2015JC011452 (2016).
Wang, B., Sullivan, L. L., and Wood, J. D., "Modeling wind-driven seed dispersal using a coupled Lagrangian particle tracking and 1-D k-ε turbulence model," Ecol. Modell. **486**, 110503 (2023).
Webster, R. D. and Shaw, R. B., "Taxonomy of the native North American species of Saccharum (Poaceae: Andropogoneae)," SIDA, Contrib. Bot. **16**(3), 551–580 (1995), see https://www.jstor.org/stable/41967160